J. Fluid Mech. (1988), *vol.* 195, *pp.* 137–159
Printed in Great Britain

On coherent structures in a highly excited mixing layer

By I. WEISBROT† AND I. WYGNANSKI†‡

† Faculty of Engineering, Tel-Aviv University, Ramat-Aviv, Tel-Aviv 69978, Israel

‡ Department of Aerospace and Mechanical Engineering, University of Arizona, Tucson, AZ 85721, USA

(Received 7 January 1985 and in revised form 19 February 1988)

The flow field in a two-dimensional mixing layer, highly disturbed by a sinusoidally oscillating flap, was mapped in order to estimate the significance of the nonlinear processes associated with the large coherent structures existing in this flow. A mixing layer which does not diverge linearly in the direction of streaming is loosely defined as being highly disturbed. Two velocity components were measured throughout the flow field using a rake of X-wire probes. Streaklines were calculated from the phase-locked measured data and were compared to pictures of smoke injected into the flow, creating a link between flow visualization and quantitative experimental results. The phase-locked vorticity and the Reynolds stresses were calculated from these measurements.

It was determined that fluctuations, locked in phase with the disturbance frequency, were not only responsible for the fast initial growth of the mixing layer but also for its contraction farther downstream (the occurrence of regions I and II in the parlance of Oster & Wygnanski 1982). The resumption of the growth of the mixing layer in region III is not controlled by the phase-locked oscillations. The first subharmonic of the imposed frequency was insignificant everywhere, and vortex amalgamation was not observed by visual means.

Detailed comparisons between experimental results and theoretical calculations, based on a linear stability model, were carried out. The theory predicted very well the normalized, cross-flow distribution of any quantity that was measured, but failed to predict the amplification rates of these quantities in the direction of streaming.

1. Introduction

The mechanism responsible for the growth of the plane turbulent mixing layer with downstream distance remains an enigma in spite of the many attempts to resolve it. There is little doubt that the spreading rate of the mixing layer is intimately related to the large coherent structures present in this flow (Brown & Roshko 1974), but a quantitative definition of these structures, their contribution to the Reynolds stress and, consequently, the mean velocity field is still unknown. These structures take the form of quasi-two-dimensional vortices, but knowledge of the vorticity distribution associated with them is sketchy since conditionally sampled data are not precisely repeatable (Browand & Weidman 1976; Hussain 1983). Vortex interactions seem to be responsible for most of the cross-stream momentum transfer, and the nature of these interactions is described in a qualitative manner commonly referred to as 'pairing' (Winant & Browand 1974). Nevertheless, the persistence of the large vortices over a vast range of Reynolds numbers and their perseverance regardless of the various attempts to destroy them (Wygnanski *et al.* 1979; Browand & Ho 1983) suggest that they play a central role in the evolution of the mixing layer. This realization spurred numerous experimental and theoretical research activities.

The turbulent mixing layer has been artificially excited (Oster *et al.* 1978; Oster & Wygnanski 1982; Ho & Huang 1982; Fiedler & Mensing 1985) for the purpose of elucidating and controlling the entrainment and growth mechanism. Vortex pairing was modelled by Patnaik, Sherman & Corcos (1976), Acton (1976), Ashurst (1979), Riley & Metcalfe (1980), Corcos & Sherman (1984) and, most recently, by Inoue & Leonard (1987). In most of these predictions, spatial periodicity was assumed in order to simplify the calculations which consider a temporal evolution of the flow; the results resemble, at least qualitatively, observations made in the laboratory using a variety of flow visualization techniques.

The evolution of the large eddies is also predicted from hydrodynamic stability theory. In laminar flows, where the mean velocity profile represents the solution of the equations of motion, one may determine the character of the disturbances resulting from the instability of the flow field. Such an analysis was done by Michalke (1964, 1965), who predicted the temporal and spatial growth of perturbations in an inviscid two-dimensional mixing layer. The mean velocity profile used in the calculations was represented by a hyperbolic-tangent function. Monkewitz & Huerre (1982) compared the stability of the 'tanh' profile with the profile resulting from the exact solution of the boundary-layer equations while investigating the influence of the velocity ratio on the spatial instability of the mixing layers. They found that the maximum amplification rate of the perturbation is approximately proportional to the parameter $R = (U_2 - U_1)/(U_2 + U_1)$, while the shape of the velocity profile was less important.

The application of the linear stability theory to turbulent flows is not straightforward, because there is no steady velocity field in existence upon which a perturbation may be superimposed. One tends to select the mean velocity profile as being representative on the average, recognizing the possibility that, at any instant in time, the actual flow may only bear a slight resemblance to the mean. Nevertheless, knowing that the random changes in the mean velocity occur on a timescale that is short in comparison with the period associated with the large coherent structures, and assuming that the kinetic energy exchange between largely disparate scales is negligible, Gaster, Kit & Wygnanski (1985, hereinafter referred to as GKW) applied the inviscid linear stability theory with a large measure of success. They modelled the development of normal modes in a slowly divergent, turbulent, mixing layer by expanding the inviscid equations in multiple scales in a way similar to the one used by Bouthier (1972) and by Crighton & Gaster (1976). The streamwise velocity component of the computed eigenfunctions agreed well with experimental results, but the quantitative comparison of the growth rates was rather poor. Since the relative merit of the stability approach over direct vortex simulation is being questioned, one of the aims of this investigation was to extend the detailed comparison with linear stability theory to quantities not hitherto compared (i.e. the lateral velocity component, the phase-locked $\langle u'v' \rangle$ product, and the spanwise vorticity distributions) and to determine the limitations of the linear approach by exciting the flow at high amplitudes.

Although large coherent structures were discovered in this flow (Brown & Roshko 1974), knowledge of the ensuing velocity and vorticity fields induced by these structures is lacking, because the primary information available is based on flow visualization rather than on quantitative measurements. Therefore, a second aim of this investigation was to develop a quantitative tool for assessing the dynamical significance of some visual observations. This was attained by calculating the streakline patterns from phase-locked velocity measurements. Provided the reconstructed structures agree with visual observations, then the same quantitative data can be used for correlating visual observations which have special significance with the phase-locked vorticity, the $\langle u'v' \rangle$ product, and any other quantity of interest.

2. A brief description of the experimental procedure

The experiments were conducted in the mixing-layer facility described by Oster & Wygnanski (1982); the velocity of the slower stream was 6 m/s; the parameter $R = (U_2-U_1)/(U_2+U_1)$ was 0.25; and a representative Reynolds number based on the velocity difference and an average momentum thickness was $Re_\theta = 5000$. The excitation was produced by a flap oscillating at a frequency of 44.5 Hz, and the measurements were taken with a rake of 7 X-wires (i.e. 14 channels of anemometry) operated at a constant temperature and calibrated in a manner described by Oster & Wygnanski. The streamwise (u) and the transverse (v) components of the velocity vector were measured at 80 cross-sections in the flow, starting from a distance $X = 200$ mm downstream of the flap, at intervals of 20 mm. The velocity at each point was sampled at 2.048 kHz for a period of 250 ms (i.e. 512 data points were stored per record per channel) and recorded on tape; 100 records were used for averaging purposes. The total averaging time was therefore 25 s, which is approximately equivalent to 1000 cycles of the excitation. In order to explore the generation of the phase-locked subharmonic frequency (perhaps resulting from the pairing process), 16 channels of data were recorded simultaneously; 14 channels of anemometry, 1 channel of the sinusoidal signal activating the flap, and an additional channel of a synchronized square-wave signal produced by an electronic frequency-dividing network (i.e. the frequency of the square wave is precisely one-half of the flap excitation frequency). The square wave and the sine wave were used independently to obtain phase-locked averages. A fast-Fourier-transform algorithm was used to calculate the power spectra and the cross-spectra of the $u'v'$ product at various locations in the flow.

3. The mean velocity in the highly excited shear layer

The flow is described statistically by averaging the data obtained at each location with respect to time. The mixing layer width, b, was estimated from the mean velocity profile measured at each cross-section as follows:

$$b = (Y_{0.95} - Y_{0.10}),$$

where $Y_{0.95}$ and $Y_{0.10}$ are the lateral coordinates at which $(\bar{U}-U_1)/(U_2-U_1) = 0.95$ and 0.10, respectively. The momentum thickness θ,

$$\theta = (U_2-U_1)^{-2} \int_{-\infty}^{\infty} (U_2-\bar{U})(\bar{U}-U_1)\,\mathrm{d}Y,$$

was also computed. The dependence of b and θ on X is shown in figure 1, and the variation of $Y_{0.95}$, $Y_{0.5}$, and $Y_{0.1}$ with the distance from the splitter plate is plotted in figure 2. The dense grid of data points was necessary in order to achieve satisfactory resolution for the calculation of streaklines. Unlike the undisturbed and the slightly

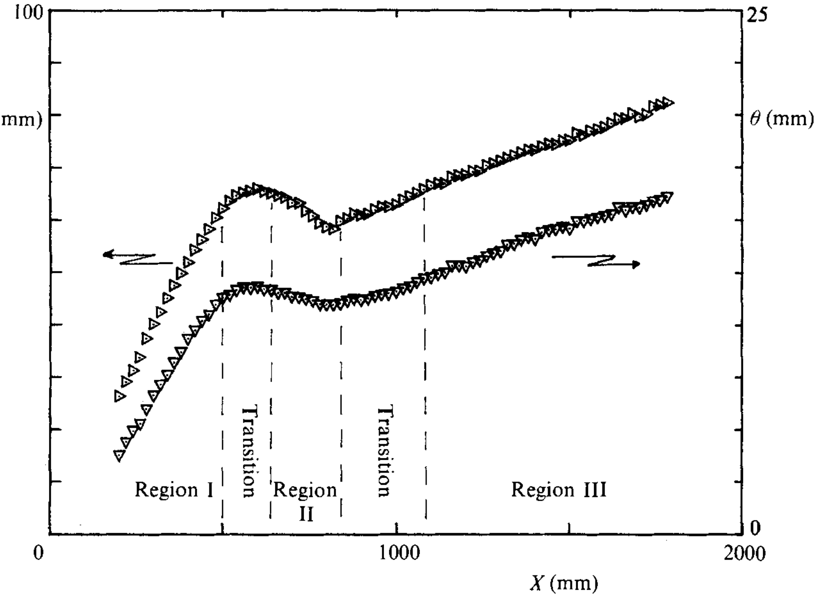

FIGURE 1. The variation of the momentum thickness, θ, and the width of the mixing layer, b, with distance from the splitter plate.

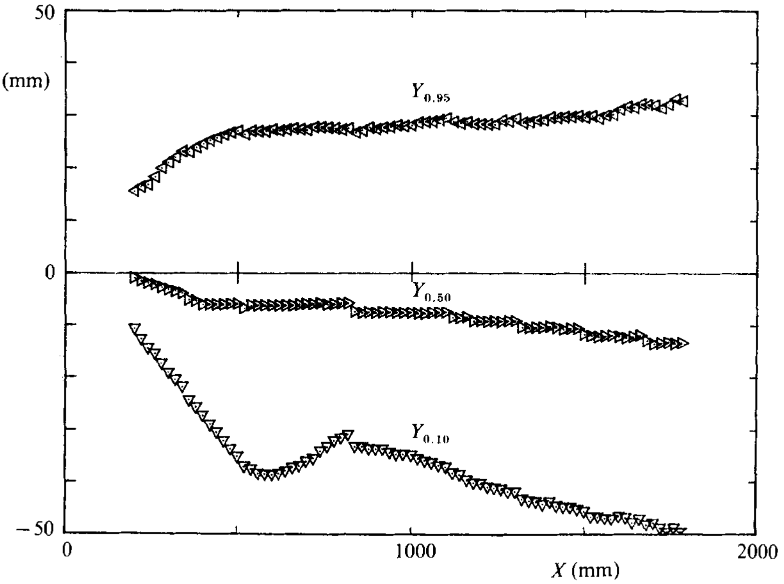

FIGURE 2. The variation of $Y_{0.10}$, $Y_{0.50}$, and $Y_{0.95}$ with distance from the splitter plate.

excited turbulent mixing layers (GKW), the highly excited mixing layer does not spread linearly with X. Three distinct regions can be recognized in this case:

(*a*) Region I ($X < 560$ mm) in which the momentum thickness increases with increasing distance from the splitter plate. Most of region I ($X < 500$ mm) is characterized by a linear growth of the momentum thickness having a slope of $\mathrm{d}\theta/\mathrm{d}X = 0.0265$.

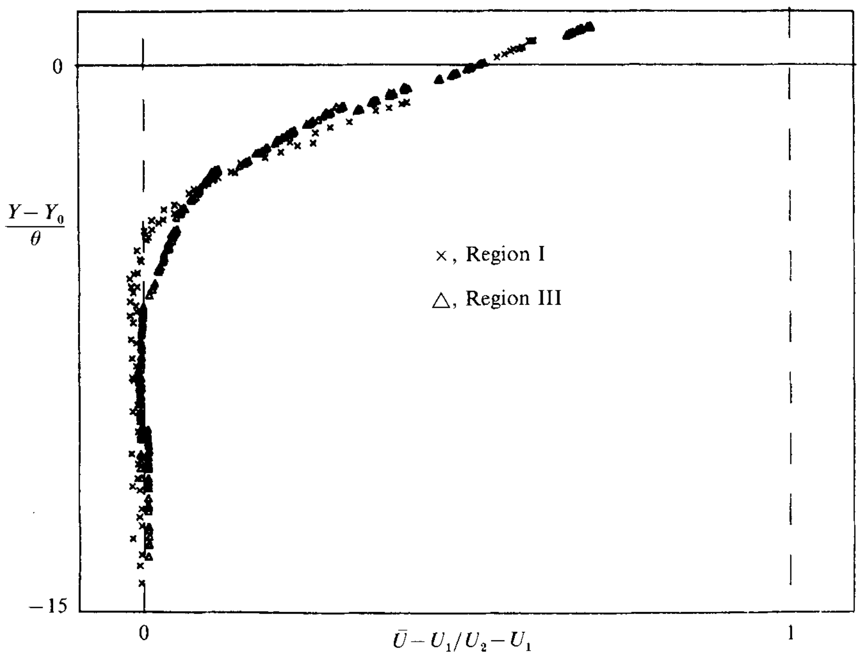

FIGURE 3. A comparison between the normalized mean velocities near the slower stream in regions I and III.

(*b*) Region II ($560 < X < 840$ mm) in which the width of the mixing layer actually decreases.

(*c*) Region III ($X > 840$ mm) in which the mixing layer resumes its linear growth, but at a much slower rate ($\mathrm{d}\theta/\mathrm{d}X = 0.0071$). At $X > 1500$ mm, the momentum thickness of the excited shear layer approaches the natural value of θ measured by Oster & Wygnanski (1982).

Two transition subregions, which will be discussed later, separate the three clearly identifiable regions. A similar behaviour of the strongly disturbed mixing layer was described by Oster & Wygnanski (1982).

The mean velocity profiles scaled by the local momentum thickness are self-similar in region I and in region III. The actual shape of the profiles changes from region to region, particularly on the low-speed side of the flow (figures 2 and 3) where

$$\left[\frac{1}{\theta}\frac{\mathrm{d}\bar{U}}{\mathrm{d}Y}\right]_{\text{region I}} > \left[\frac{1}{\theta}\frac{\mathrm{d}\bar{U}}{\mathrm{d}Y}\right]_{\text{region III}} \quad \text{for } \bar{U} > U_1.$$

The difference in the shape of the mean velocity profiles cannot be attributed to an experimental inaccuracy and must stem from the dynamics of the energy-containing eddies. It should be noted that other definitions of the width of the mixing layer, such as the maximum-slope (or vorticity) thickness $\delta_w = (U_2-U_1)/(\mathrm{d}\bar{U}/\mathrm{d}Y)_{\max}$ (Brown & Roshko 1974), are not sensitive to the variations in the shape of the mean velocity profiles.

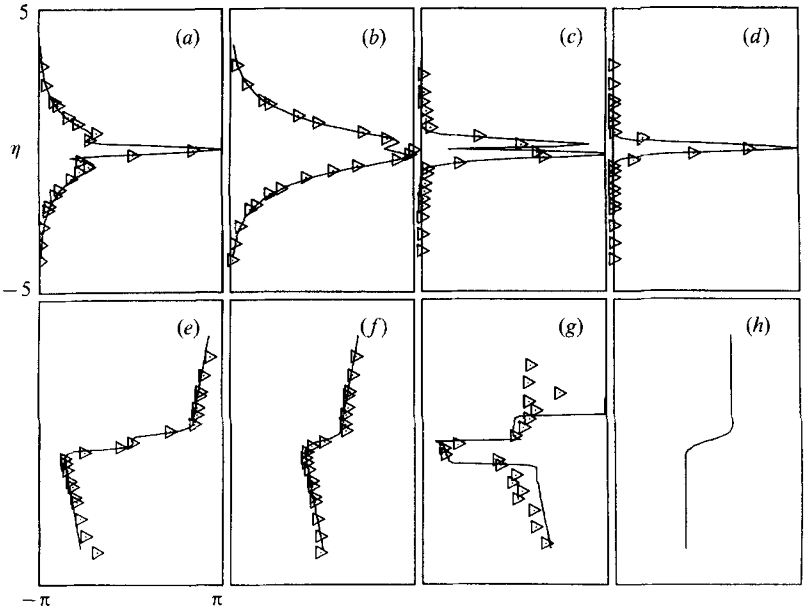

FIGURE 4. The lateral distributions of normalized amplitudes and phases of the ensemble-averaged fluctuations measured at $X = 200$ mm and filtered at the excitation frequency. (a)–(c) show the amplitudes of $\langle u' \rangle_f, \langle v' \rangle_f, \langle \Omega' \rangle_f$; and (d) is the cross-product $\langle u'v' \rangle_f$. (e)–(g) show the phase of $\langle u' \rangle_f, \langle v' \rangle_f, \langle \Omega' \rangle_f$, and (h) is the mean velocity profile measured at this X-location. The solid lines in (a)–(g) represent a theoretical prediction while the triangular symbols represent experimental data.

4. The applicability of linear stability theory to region I

The linear, inviscid stability theory provides a powerful tool in modelling the development of slightly disturbed flows. GKW applied this model to a turbulent, slowly diverging, mixing layer and compared the theoretical calculations for the streamwise velocity component with experimental results. Although the lateral distributions of phase angles and the normalized amplitudes showed good agreement with the model, the predicted amplification rate exceeded the experimental observations. A partial purpose of this experiment was to increase the excitation level until the harmonic distortion became significant and $\mathrm{d}\theta/\mathrm{d}X$ was no longer constant throughout, and to observe the shortcomings of the linear theory as it was applied to region I. The measurements were also extended to include two velocity components from which phase-locked vorticity and the $\langle -u'v' \rangle$ product were calculated. All measurements were compared with the theoretical calculations described by GKW. The shape of the normalized mean velocity profile was almost identical in both investigations over the distances of interest and, therefore, the functional description of the profile was retained; the rate of spread ($\mathrm{d}\theta/\mathrm{d}X$) used in the present calculations was different, however. Some of the notation used in figures 4–6 was defined by GKW; in particular, the variable ξ describes a dimensionless streamwise coordinate which also incorporates the slight variation of the thickness of the mixing layer in the direction of streaming (see equation (5.3) of GKW). This variable is equal to unity where the mixing layer is neutrally stable with respect to the imposed circular frequency β. The normalized lateral distributions of the amplitudes of $\langle u' \rangle_f, \langle v' \rangle_f, \langle \Omega' \rangle_f = \partial \langle u' \rangle_f / \partial Y - \partial \langle v' \rangle_f / \partial X$ at the excitation frequency

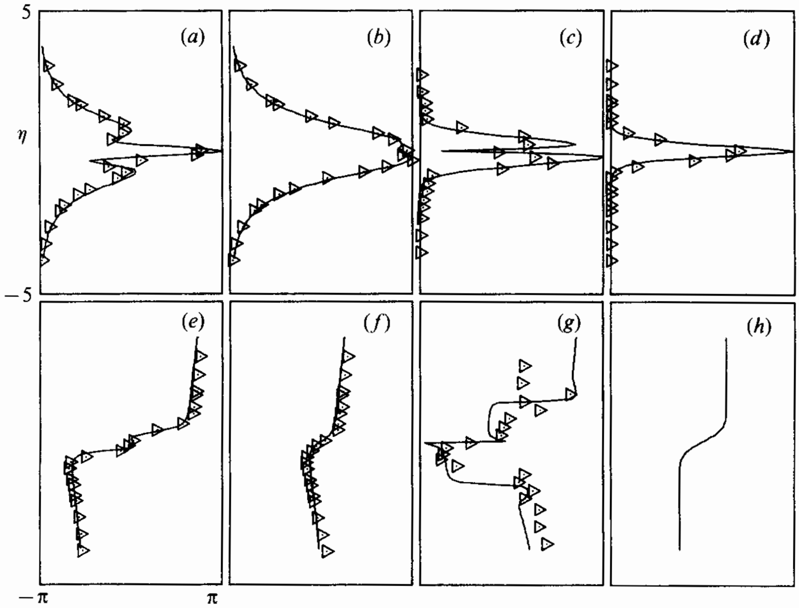

FIGURE 5. As for figure 4 but measured and computed for X = 300 mm.

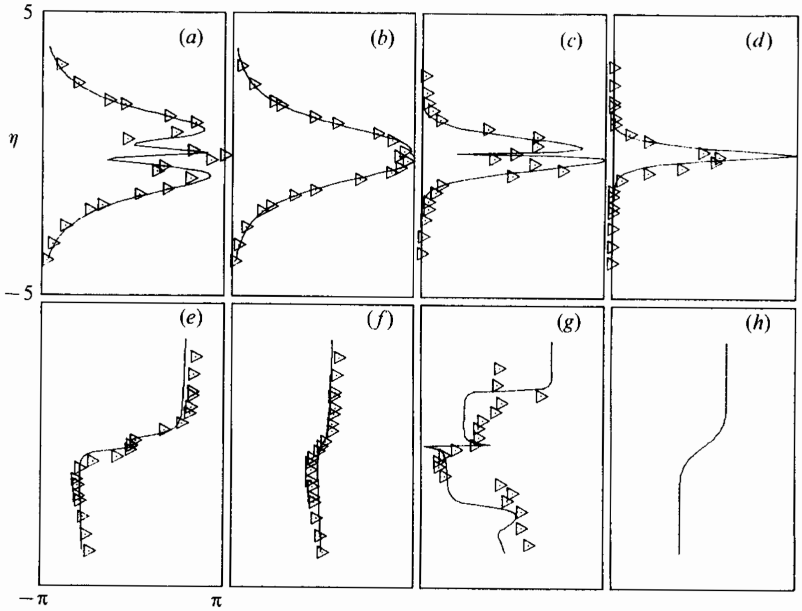

FIGURE 6. As for figure 4 but measured and computed for X = 400 mm.

and their respective phase angles are plotted in figures 4–6 for $X = 200$, 300, and 400 mm ($\xi = 0.293, 0.543, 0.793$, respectively). The mean velocity profile drawn to the same scale is plotted on these figures for comparison. The distributions of the spanwise vorticity component were computed by numerical differentiation of the neighbouring phase-locked velocity vectors which were Fourier transformed after the differentiation.

The triangles in all the figures represent experimental results, while the theoretical predictions at a corresponding dimensionless streamwise distance are marked by solid curves. The amplitude distribution of any quantity Q in figures 4–6 was normalized by the local integral $\int_{-\infty}^{\infty} Q\,\mathrm{d}\eta$, where $\eta=(Y-Y_{0.5})/\theta$. The phase distributions were matched at a single arbitrary point at $\eta=0$. The good agreement between all the calculated and measured quantities indicates that the linear inviscid theory serves as a good first step in predicting the nature of the disturbances in region I of a turbulent mixing layer.

At $X=200$ mm, the distribution of $\langle u'\rangle_f$ has a strong, but narrow peak around $\eta=0$, flanked by two lobes having a maximum amplitude equivalent to 25% of the peak and extending to $\eta=\pm 3$. At $X=300$ mm, the side lobes approach 50% of the peak and, at $X=400$ mm, they are equal to it. The lateral distribution of $\langle v'\rangle_f$ is broad and retains its general shape at all distances considered. The lateral distribution of $\langle u'v'\rangle_f$ is very narrow and is concentrated around $\eta=0$. A statistical approach to turbulent flow would suggest that the fluctuations in u and v are uncorrelated, but according to linear and inviscid stability theory, the perturbation stream function ψ decays exponentially with Y whenever $\mathrm{d}^2U/\mathrm{d}Y^2\rightarrow 0$, resulting in a rapid decay of the second-order product $\langle u'v'\rangle_f$ in the lateral direction (i.e. $\langle u'v'\rangle_f=-\alpha\,\mathrm{e}^{-\alpha Y}$, where α is the eigenvalue whose real part corresponds to the wavenumber). The measured and the calculated vorticity perturbation profiles have a minimum at or near $\eta=0$ where $\bar{U}''$ vanishes. According to the linear inviscid stability model, the perturbation vorticity $\langle \Omega'\rangle_f$ is given by

$$\langle \Omega'(y)\rangle_f=-\frac{\bar{U}''}{U-\beta/\alpha}\phi$$

and therefore it has to vanish whenever $U''=0$, provided either α or β is complex. In the neutral case ($\xi=1$), the ratio $\bar{U}''/(U-\beta/\alpha)$ does not vanish whenever $(\bar{U}-\beta/\alpha)\rightarrow 0$, and the lateral distribution of vorticity changes from having two vortex cores, separated by a minimum corresponding to the location at which $U''=0$, to having a single vortex core at the same lateral location (Michalke 1965). The unification of the two vorticity cores at the excitation frequency may be synonymous with the pairing process, and it occurs experimentally at $X\approx 500$ mm. A detailed discussion of pairing is presented in Wygnanski & Weisbrot (1988).

The overall amplification of the longitudinal velocity in the streamwise direction is represented by $\int_{-\infty}^{\infty} |\langle u'\rangle_f|\,\mathrm{d}\eta$ and shown in figure 7(*a*). The corresponding integral for the lateral velocity component in figure 7(*b*), while the spanwise vorticity perturbation is shown in figure 7(*c*). All the figures are plotted on semilogarithmic coordinates in which the abscissa is the dimensionless streamwise coordinate ξ (for this case, the distance X mm $=(400\xi+83)$; see GKW for details) and the ordinate is the local value of the integral normalized by its local value at the first station. The triangles represent the experimental data, while the theoretical values are plotted by solid curves.

Two of the three integrals calculated theoretically increase monotonically with X, but $\int_{-\infty}^{\infty} |\Omega'|_f\,\mathrm{d}y$ decreases for $X<370$ mm, where it reverses its trend and starts to increase with increasing X. The measured amplitudes of the two velocity components also increase with X, but at a considerably slower rate. The experimental and the theoretical integrals of $|v'|_f$ increase much more rapidly with X than the corresponding integrals of $|u'|_f$ [cf. figure 7(*a*) with figure 7(*b*)]. The integral of

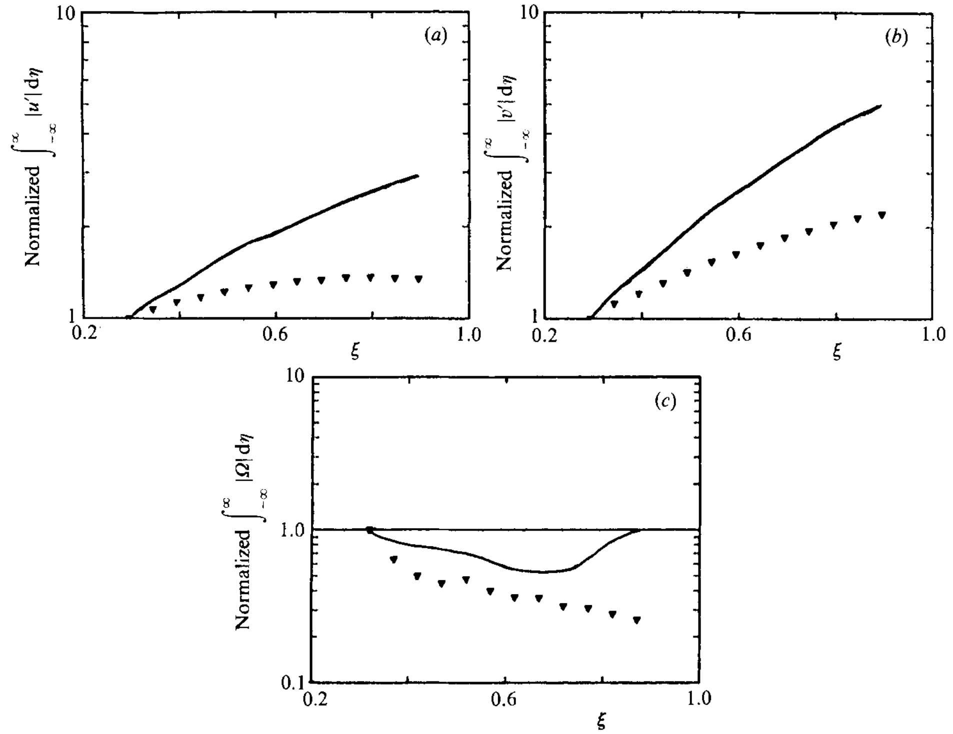

FIGURE 7. The amplification of the laterally integrated disturbances with distance from the splitter plate. Solid lines represent predictions and symbols represent experimental data:

$$(a)\ \int_{\infty}^{-\infty} |\langle u'\rangle_f|\,d\eta;\quad (b)\ \int_{-\infty}^{\infty} |\langle v'\rangle_f|\,d\eta;\quad (c)\ \int_{-\infty}^{\infty} |\langle \Omega'\rangle_f|\,d\eta.$$

the measured longitudinal velocity component tends to decrease toward the end of the domain of comparison.

The vorticity amplitude, integrated across the flow, decreases rapidly with X for $X < 260$ mm; it then remains constant over a short distance before decreasing again at $X > 320$ mm. The slopes of the measured and predicted integrals of vorticity have an opposite sign over the latter part of the domain of comparison. The discrepancy betwen the high amplification rates predicted by the linear model and the relatively low amplification rates realized in the experiment deserves special attention in view of the excellent agreement between the normalized shapes of the theoretical and experimental eigenfunctions.

The linear model used is based on the assumption that the divergence of the mean flow is *decoupled* from the maximum attainable amplitudes of the imposed perturbations. It is further assumed that the divergence of the excited shear layer is slight and represents a weak modification to the parallel stability model. The interaction between the large (externally excited) coherent structures and the background turbulence was not considered. This is not a severe handicap in region I where the turbulent energy production accounts for less than 25% of the total while the remaining 75% is attributed to the phase-locked fluctuations at the disturbance frequency and its first harmonic. The contribution of the second-order products, not accounted for in the present analysis, may actually be very significant

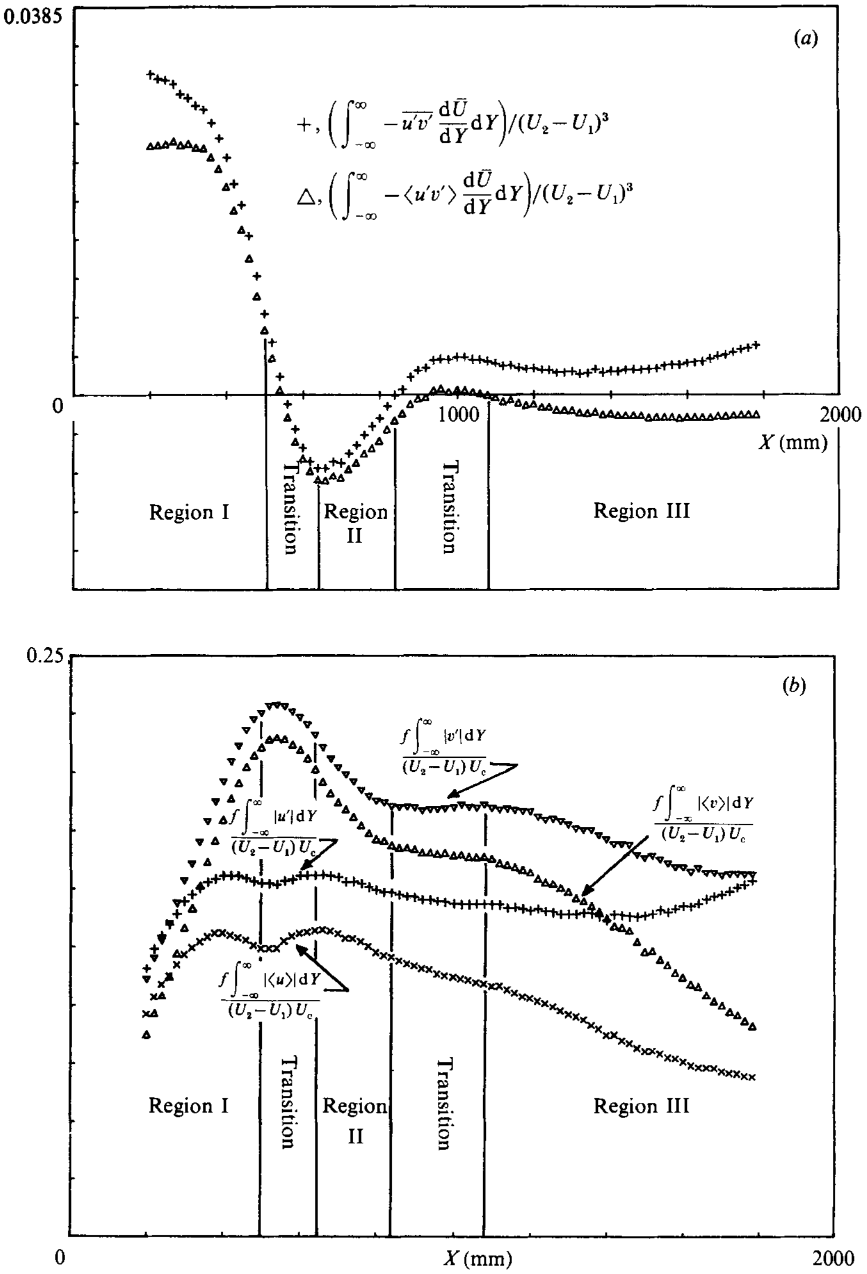

FIGURE 8(*a,b*). For caption see facing page.

and will be discussed later. GKW estimated that 45% of the overall level of the streamwise velocity fluctuations is concentrated at the excitation frequency which, in the context of the present experiment, means that at $\xi = 0.786$ where the level of $u'/(U_2-U_1) \approx 18\%$, the coherent fluctuation levels are approximately equivalent to 8% of the velocity difference and thus the linearization of the equations of motion may not be justified.

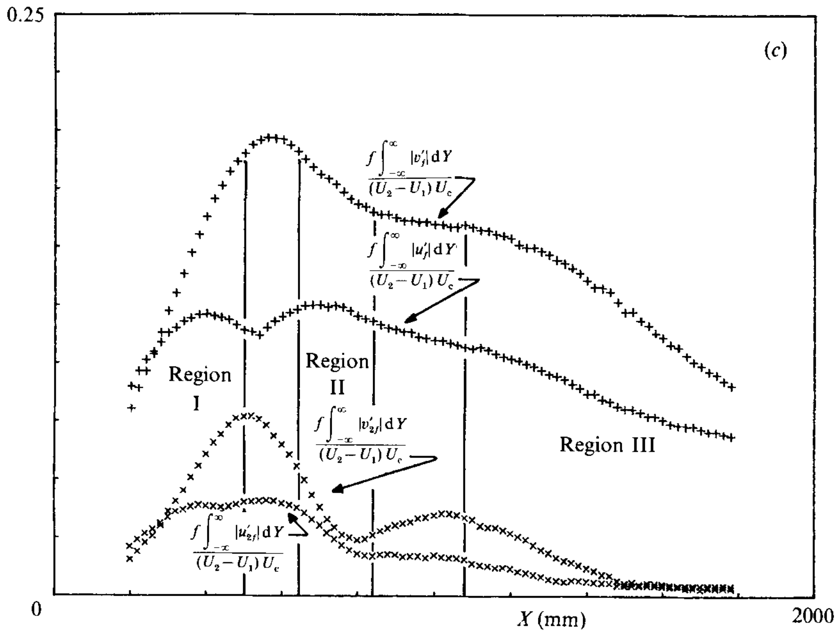

FIGURE 8. (*a*) The production of energy integrated across the flow. (*b*) The temporally averaged and ensemble-averaged amplitudes of u', $\langle u \rangle$, v', and $\langle v' \rangle$ integrated across the flow. (*c*) The amplitudes of $\langle u' \rangle_f$, $\langle u' \rangle_{2f}$, $\langle v' \rangle_f$, and $\langle v' \rangle_{2f}$ integrated across the flow.

5. The intensity of the fluctuations, the Reynolds stress, and their respective spectral distributions

The Reynolds stress ($\tau = -\rho u'v'$) is linked to the mean momentum equation and to the mean kinetic-energy equation; therefore, changes in the distribution of $-u'v'$ are associated with changes in the momentum thickness θ and with the exchange of energy between the fluctuations and the mean motion. The overall energy production term can be subdivided into a phase-locked (coherent) term and a random (turbulent) term. The reader is referred to Hussain's (1983) article discussing the triple velocity decomposition.

The production of energy integrated across the flow is shown in figure 8(*a*) as a function of the streamwise distance. The overall production term (marked by crosses) and the phase-locked production term (obtained from the product $-\langle u'v' \rangle\, d\bar{U}/dY$ and marked by triangles) are plotted together in order to relate the energy production and the Reynolds stress to the divergence of the shear layer. The corresponding amplitudes of the phase-locked $u'$and v' fluctuations integrated across the flow are shown in figure 8(*b*), while the integrals of these fluctuations *at the excitation frequency* and its first harmonic ($2f$) are plotted in figure 8(*c*). These plots are helpful in delineating the most significant terms contributing to the failure of the linear model and will be discussed later.

5.1. *Region I*

A typical transverse distribution of Reynolds stress measured in the portion of region I in which $d\theta/dX$ is constant (i.e. $X < 500$ mm) is shown in figure 9. The data are compared with the phase-locked $-\langle u'v' \rangle$ product, marked by triangles on the same

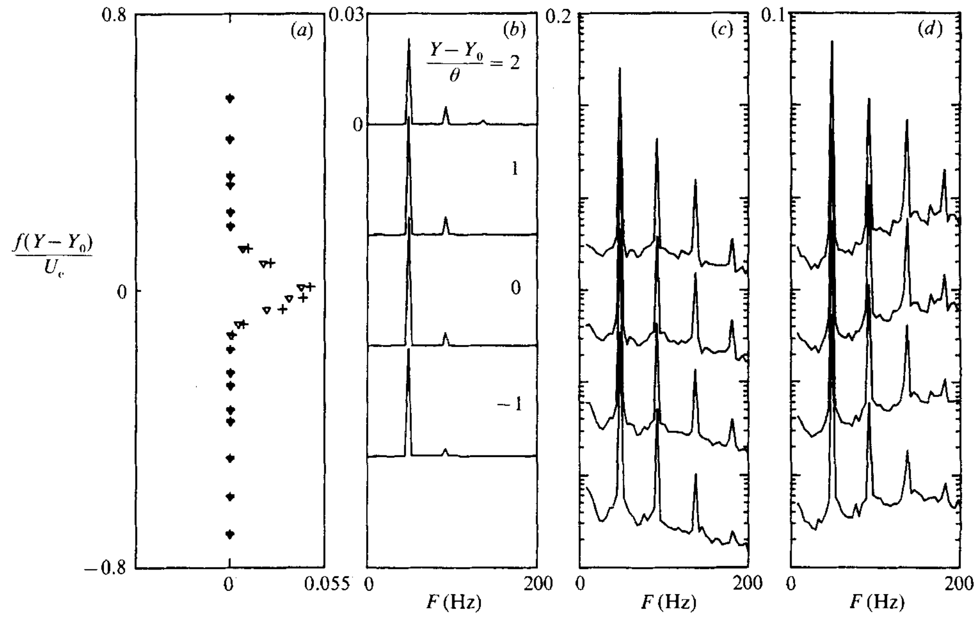

FIGURE 9. The transverse distribution of (*a*) Reynolds stress: +, $-\overline{u'v'}/(U_2-U_1)^2$; ▽, $-\langle u'v'\rangle/(U_2-U_1)^2$; (*b*) the cross-spectra of $u'v'$: $S_{uv}/(U_2-U_1)^2$; and (*c, d*) the power spectra of u' and v': $S_{u^2}/(U_2-U_1)^2$; $S_{v^2}/(U_2-U_1)^2$, at $X = 280$ mm.

figure; the latter obviously accounts for most of the Reynolds stress. Temporally averaged and phase-locked-averaged energy production terms behave in a similar manner, suggesting that the flow is governed by the phase-locked fluctuations. Graphs representing the cross-spectra measured at four lateral locations ($\eta = 2, 1, 0, -1$) at the same streamwise distance show that the disturbance frequency dominates the flow in spite of the fact that the first harmonic may also be detected. Higher harmonics do appear in the power spectra of the longitudinal and lateral velocity components, but they are not sufficiently strong or sufficiently correlated to influence the Reynolds stress.

The harmonic distortion, defined as the ratio between the energy contained in the harmonic frequency to the energy contained at the excitation frequency, may be deduced from figure 9. The harmonic distortion of the streamwise component of velocity at $X = 200$ mm and $(Y-Y_0)/\theta = 2$ is approximately 0.06, and it increases by an order of magnitude between $X = 200$ mm and $X = 400$ mm at the outer peripheries of the shear layer; it does not increase at $(Y-Y_0)/\theta = 0$. The harmonic distortion of the lateral velocity component increases by a factor of 2 over the same distance and does so uniformly across the shear layer. The initial increase in the harmonic distortion with downstream distance may not necessarily imply that the nonlinear terms in the equation of motion are important in region I. It may simply indicate that the harmonic content introduced inadvertently by the flap amplifies linearly at a faster rate than the fundamental, because the mixing layer is initially thin. This suggestion, however, can easily be refuted because:

(i) The integrated amplitudes of $|u'_{2f}|$ and $|v'_{2f}|$ keep increasing throughout region I (figure 8*c*) in spite of the fact that, according to the linear model, their amplification should have ceased at $X = 300$ mm. At this location, the shear layer became neutrally stable to the harmonic frequency.

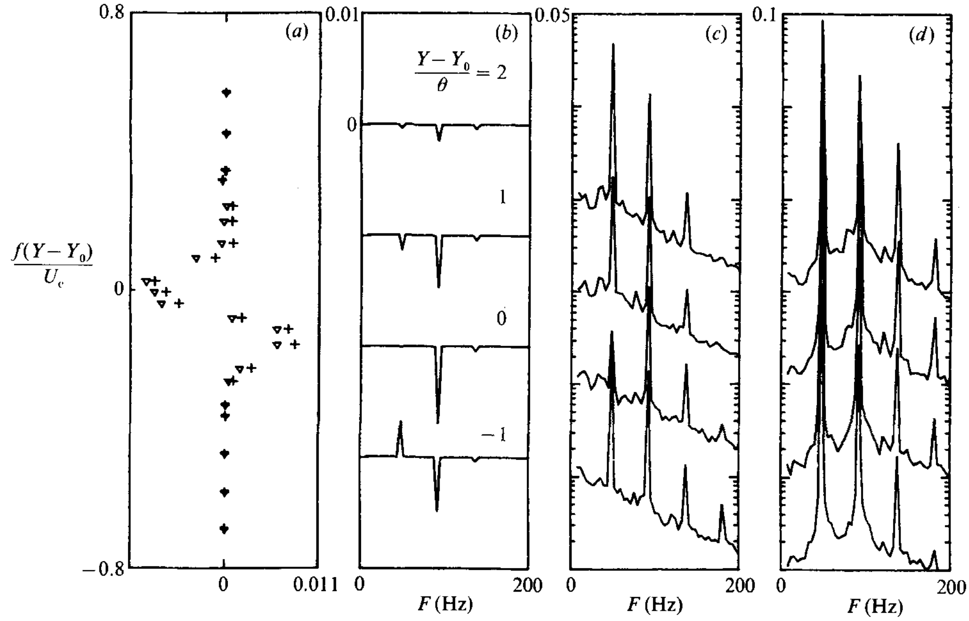

FIGURE 10. As figure 9 but at $X = 560$ mm.

(ii) The integrated amplitude of $|v'|_f$ increases in region I by a factor of 2.3 from the first cross-section measured at $X = 200$ mm to $X = 500$ mm (see also figure 7). The integrated amplitude of $|v'_{2f}|$ increases by a factor of 5.3 over the same distance. The amplification rate of $|v'_{2f}|$ is almost identically equal to the square of the amplification ratio of $|v'_f|$, suggesting that $|v'|_{2f}$ is generated by the first-order nonlinear interaction. A similar observation can be made with respect to the streamwise component of the fluctuation in the region $200 \leqslant X \leqslant 400$ mm since, in this case, the integral of $|u'_f|$ attains its maximum at $X = 400$ mm (figure 8c).

(iii) The distribution of $|v'|_{2f}$ and $|u'|_{2f}$ across the flow is not well predicted by the linear stability eigenfunction.

5.2. *The first transition subregion*

The first transition subregion ($500 < X < 640$ mm) is defined as the region in which $\mathrm{d}\theta/\mathrm{d}X$ changes from its constant positive value in region I to a constant negative value in region II. A local maximum of the momentum thickness is attained at $X = 560$ mm, where the overall turbulent energy production vanishes (figure 8a), the integrated intensity of the transverse fluctuations $|v'|$ attains a maximum, and the integral of $|u'|$ has a local minimum (figure 8b). The end of this transition subregion corresponds to a minimum in the overall turbulent production ($X = 640$ mm). A second maximum of the integrated streamwise component of the fluctuations also occurs at $X = 640$ mm (figure 8b) stemming from a favourable phase relationship between $|u'_f|$ and $|u'_{2f}|$ since none has a maximum at this location (figure 8c).

The distributions of $-u'v'$ and $\langle -u'v' \rangle$, as well as the corresponding energy production terms, are almost equal in this subregion (figure 10), as might have been expected from figure 8(a). Consequently, the flow continues to be dominated by the excitation frequency. The Reynolds stresses and the concomitant production terms change sign to become negative. The change is initially observed on the high-velocity side of the flow and is associated with the increased inclination of the large vortices

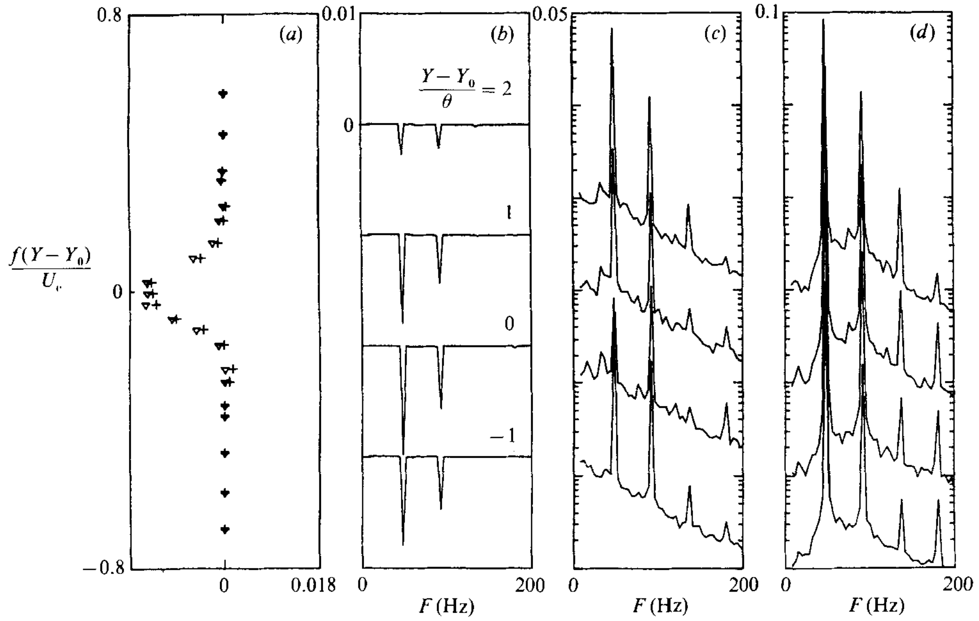

FIGURE 11. As figure 9 but at $X = 640$ mm.

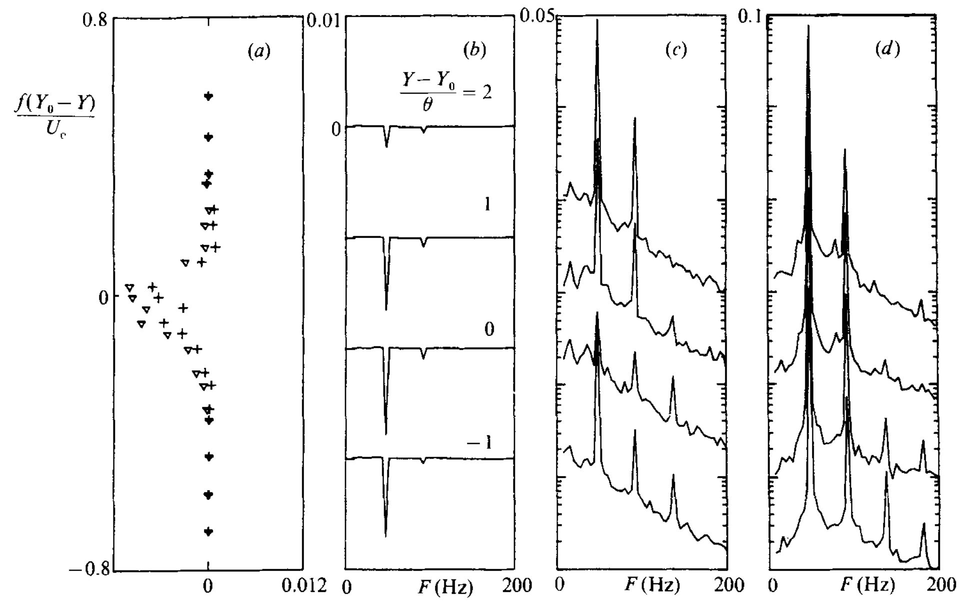

FIGURE 12. As figure 9 but at $X = 780$ mm.

(see Ho & Huerre 1984, figures 20 and 21) resulting from the comparatively larger phase velocity in this region (see figures 4 and 5 in GKW).

The first harmonic of the cross-spectrum, which has an amplitude comparable with the amplitude of the imposed frequency, changes its sign first, and the fundamental frequency follows (figure 11). The interaction between the imposed fluctuations and their first harmonic frequency appears to be the dominant factor responsible for the

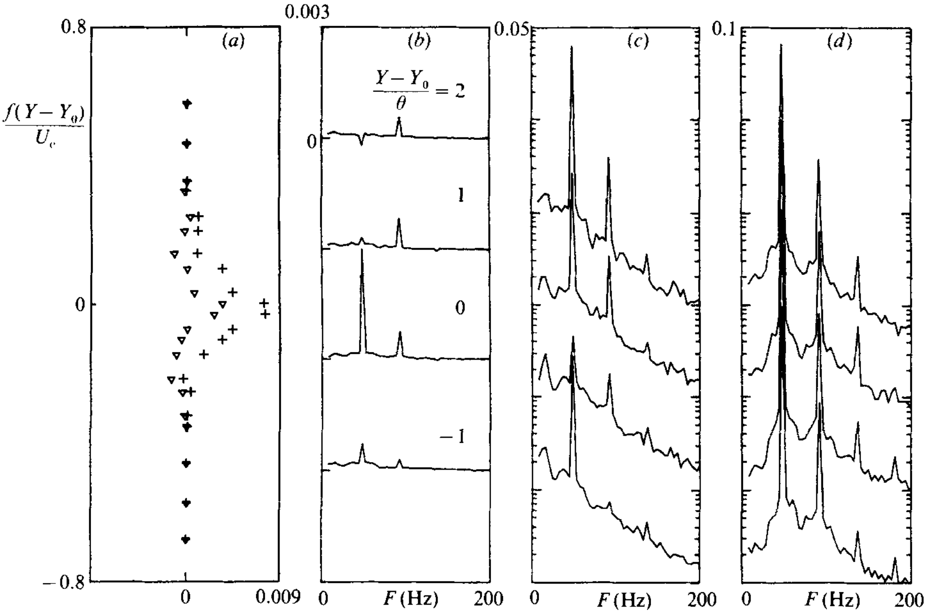

FIGURE 13. As figure 9 but at X = 940 mm.

contraction of the mixing layer with downstream distance. The harmonic distortion of the longitudinal and the lateral velocity components diminishes in this region, particularly on the high-velocity side of the flow. It is interesting to note that the integral across the flow of $|u'_f|$ is amplified between X = 520 mm and X = 700 mm, while the corresponding integral of $|v'_f|$ diminishes (figure 8*c*). The integral of $|v'_{2f}|$ decreases steeply in this region.

5.3. *Region II*

In region II ($640 < X < 840$ mm), the momentum thickness of the mixing layer decreases. The overall energy production is negative (figure 8*a*), and the inclination angle of the vortices on the high-speed side of the flow decreases. The phase-locked oscillations still dominate the flow (figure 12) and the phase-locked energy production throughout the region is negative (figure 8*a*). The cross-stream integrals of $|u'_f|$, $|u'_{2f}|$, $|v'_f|$, and $|v'_{2f}|$ also decrease (figure 8*c*).

The flow in this region appears to be dominated by the large vortices which are perfectly locked to the phase of the flap motion (see also Oster *et al.* 1978). Although the products of $u'v'\,\mathrm{d}\bar{U}/\mathrm{d}Y$ and of $\langle u'v'\rangle\,\mathrm{d}\bar{U}/\mathrm{d}Y$ are negative throughout, suggesting that energy is lost by the large eddies to the mean motion, the integral $\int_{-\infty}^{\infty}|u'|\,\mathrm{d}y$ hardly diminishes between $660 < X < 800$ mm (figure 8*b*) while the integrated harmonic component of $|u'_{2f}|$ and $|v'_{2f}|$ diminishes greatly over the corresponding distance. The harmonic distortion of u', which is 0.5 at $X = 440$ mm and $(Y-Y_0)/\theta = 2$, is reduced to 0.05 at a corresponding lateral location at X = 840 mm. The second harmonic ($F = 3f$), which is significant in region I (figures 9 and 10), disappears completely in region II, and most of the random fluctuations are shifted toward frequencies that are lower than the excitation frequency (figures 12 and 13). At X = 200 mm, the background spectral distribution of u'^2 in the range between 0 and 200 Hz is flat, while the spectrum of v'^2 slopes upward toward higher frequencies.

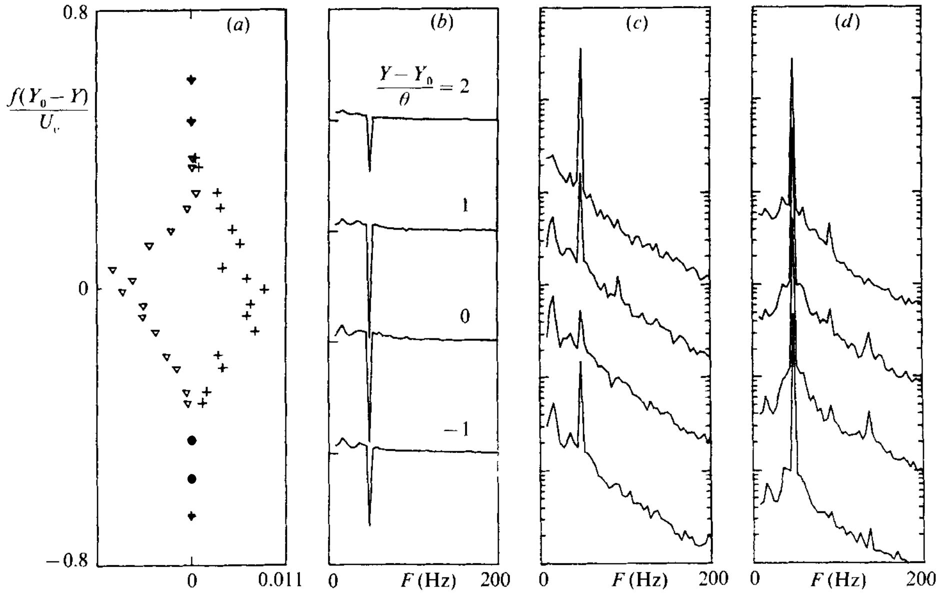

FIGURE 14. As figure 9 but at $X = 1500$ mm.

At $X = 560$ mm, the spectrum of v'^2 still has a broad-band maximum around the first harmonic frequency $2f$. At $X = 780$ mm, this maximum shifts toward the excitation frequency and remains there until the end of region II (figure 12). The cross-spectrum has two negative peaks at the excitation frequency and at its first harmonic between $600 < X < 840$ mm. The relative importance of the first harmonic of the $\langle -u'v' \rangle$ product decreases with increasing X, in this region, until it vanishes across the entire mixing layer at $X = 840$ mm; the $\langle -u'v' \rangle$ product at the excitation frequency becomes negative at $X = 600$ mm and remains negative until $X = 900$ mm.

5.4. *The second transition region*

The transition from region II to III ($840 < X < 1080$ mm) is marked by a renewed growth of the momentum thickness with increasing X and a positive overall production of turbulent energy. In this region, one may observe that the phase-locked $\langle u'v' \rangle$ product and the associated production of fluctuating energy deviate significantly from the time-averaged $-u'v'$ product and overall energy production (figure 13). While the overall production is positive, the phase-locked production of energy is negligibly small (figure 8*a*). Positive values do appear in the phase-locked $\langle -u'v' \rangle$ product in the central region of the mixing layer, but their influence is offset by the negative values at the peripheries. Positive peaks in the cross-spectra appear in both the disturbance frequency and its first harmonic in the vicinity of $(Y - Y_0)/\theta = 0$ (figure 13).

The spectral distributions of u'^2 and v'^2 do not change appreciably between $880 < X < 1080$ mm; the harmonic distortion coefficient remains constant, and the background turbulence in the spectrum of the transverse fluctuations has a broad-band maximum around the excitation frequency. Since the momentum thickness in this region is smaller than the maximum θ attained at the end of region I, one could argue that the mixing layer returns to being linearly unstable to the excitation

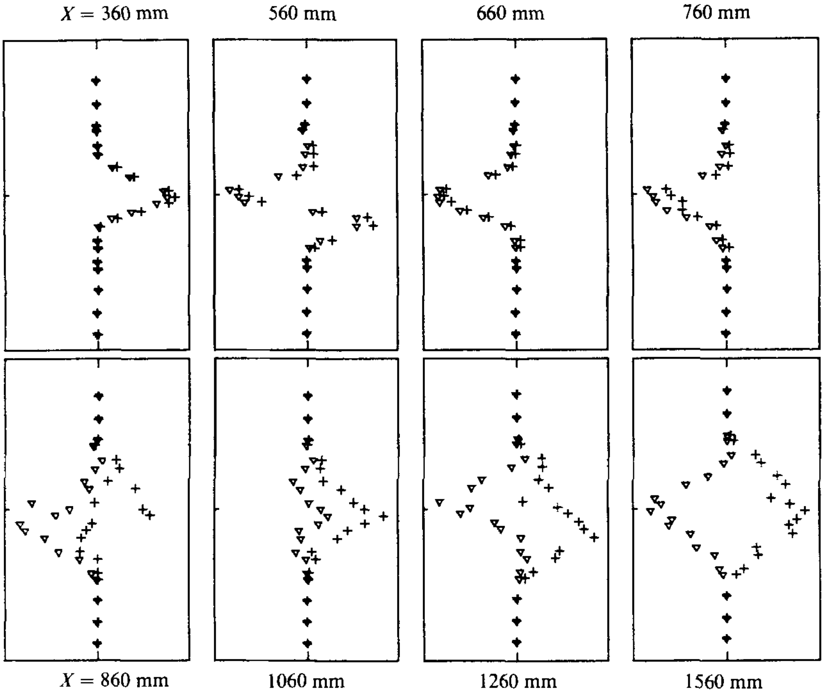

FIGURE 15. The transverse distributions of phase-locked and temporally averaged Reynolds stress at eight streamwise locations.

frequency. This is unlikely, in spite of the reappearance of positive phase-locked $\langle -u'v'\rangle$, because the integrals

$$\int_{-\infty}^{\infty} |\langle u'\rangle_f|\,\mathrm{d}y \quad \text{and} \quad \int_{-\infty}^{\infty} |\langle v'\rangle_f|\,\mathrm{d}y$$

are decreasing in this region while $\int_{-\infty}^{\infty} |\langle u'\rangle_{2f}|\,\mathrm{d}y$ increase. The increase of the amplitudes of the transverse fluctuations at the harmonic frequency cannot be attributed to a linear process but rather to a nonlinear interaction among the energetic eddies produced by the excitation. One may also recall that the mean velocity profile changes its shape in this region (figure 3).

5.5. *Region III*

In region III ($X > 1080$ mm), the mixing layer resumes its linear rate of spread with X. The growth rate in this case is approximately one-quarter of the growth rate in region I. The overall energy production in this region is positive everywhere (figure 8*a*), and the $-\overline{u'v'}$ profiles are positive (figure 14). On the other hand, the phase-locked $\langle -u'v'\rangle$ distributions are negative in this region and, consequently, the integral of $\langle -u'v'\rangle \mathrm{d}\bar{U}/\mathrm{d}Y$ is negative (figure 8*a*). The positive turbulence production stems from a broad-band, slightly positive $-u'v'$ product appearing at low frequencies and overwhelming, in the integral sense, the strong, negative cross-spectral peaks occurring at the excitation frequency (figure 14). The intensity of the phase-locked fluctuations at the harmonic frequency decreases with downstream distance for $X > 1100$ mm; only the lowest frequencies in the background increase between $1000 < X < 1700$ mm (cf. figures 13 and 14).

The distributions of $u'v'$ at 8 different streamwise locations are plotted in figure 15 as a challenge to potential modellers of this flow.

One may conclude that eddies which are larger than the eddies associated with the excitation frequency become dominant in region III. These eddies, which are not locked in-phase to the imposed oscillations, are presumably responsible for the resumed growth of the shear layer. The integrated intensity of the transverse fluctuations decreases in region III, while the integrated intensity of $|u'|$ across the flow increases for $X > 1500$ mm. At $X = 1800$ mm, the integrated phase-locked fluctuations are reduced to 50% of the corresponding temporally averaged intensities (figure 8*b*).

5.6. *The subharmonic frequency*

Anticipating that the resumed growth of the mixing layer in region III stems from vortex pairing, special attention was paid to this process and to the generation of the subharmonic frequencies. Since the large eddies passing through region II were locked to the phase of the excitation, it was assumed that the pairing process would follow suit and, therefore, the phase-averaging was done at the subharmonic frequency (see also §2). A comparison between the data phase-locked to the excitation signal, or to its subharmonic, could not be distinguished, suggesting that the process, if it exists, occurs randomly in time or space. Power spectra of u'^2 and v'^2 and the cross-spectrum of $u'v'$ reveal interesting exchanges between the excitation frequency and its harmonic component ($F = 2f$) in regions I and II and a good portion of region III (up to $X = 1300$ mm), but they do not show a clear dominance of a subharmonic frequency ($F = f/2$) as was initially anticipated (figure 14). Comparing the v'^2 spectrum shown in figure 12 (taken at $X = 780$ mm and $(Y - Y_0)/\theta = 2$) with a corresponding spectrum in figure 14 ($X = 1500$ mm), one notices:

(i) the disappearance of peaks at the harmonic frequency at $X = 1500$ mm;

(ii) the disappearance of the side bands (i.e. the broadening of the spectrum) near the excitation frequency; and

(iii) a significant increase (by an order of magnitude) of the background level of all frequencies that are lower than the excitation frequency.

6. Streaklines and vorticity distribution

One of the objectives of this work was to compare streaklines computed from the two components of the measured phase-locked velocity with conventional flow visualization techniques. Such a comparison can provide a link between qualitative observations and quantitative data and may serve as a tool for analysing the dynamic significance of 'pairing' which was first observed by Winant & Browand (1974), who injected dye into the flow.

A comparison between a streakline pattern and a smoke picture is presented in figure 16, and the resemblance between the two is obvious. In order to take the photograph, a smoke filament was introduced near the trailing edge of the splitter plate while the test section was illuminated by a stroboscope synchronized with the frequency of the flap. The exposure time was 0.8 s and, therefore, the photograph represents a phase-locked superposition of 36 events. The data used for calculating streaklines were also used for calculating the velocity and vorticity fields, the distribution of Reynolds stresses, and the exchange of energy between the mean

400 X(mm) 1160

FIGURE 16. The phase-locked structures: (*a*) smoke-illuminated stroboscopically (exposure time = 0.8 s); (*b*) calculated streaklines; (*c*) calculated isodynes.

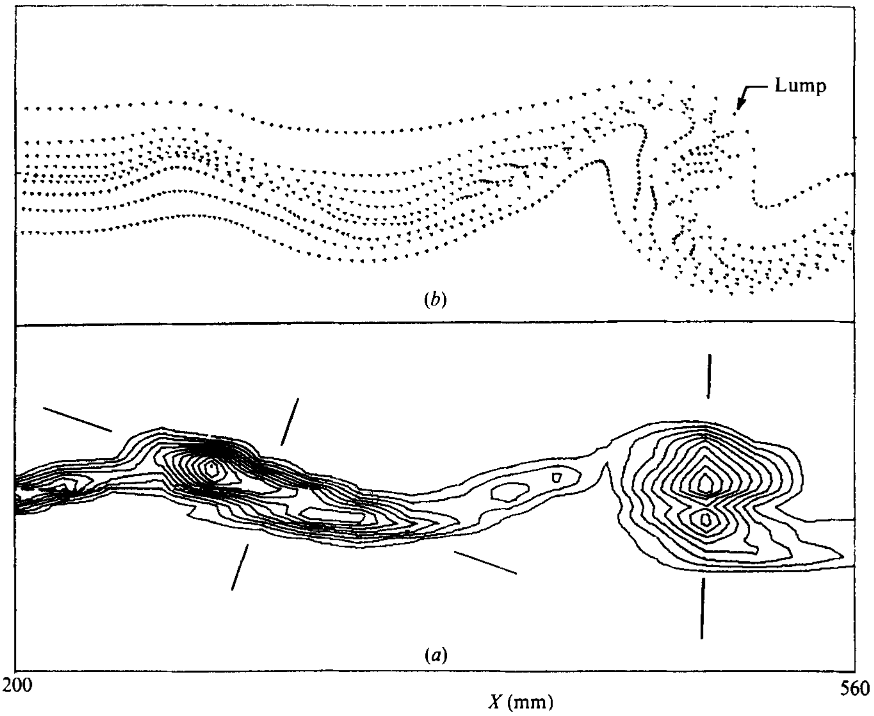

FIGURE 17. The phase-locked structures in region I: (*a*) calculated streaklines; (*b*) calculated isodynes.

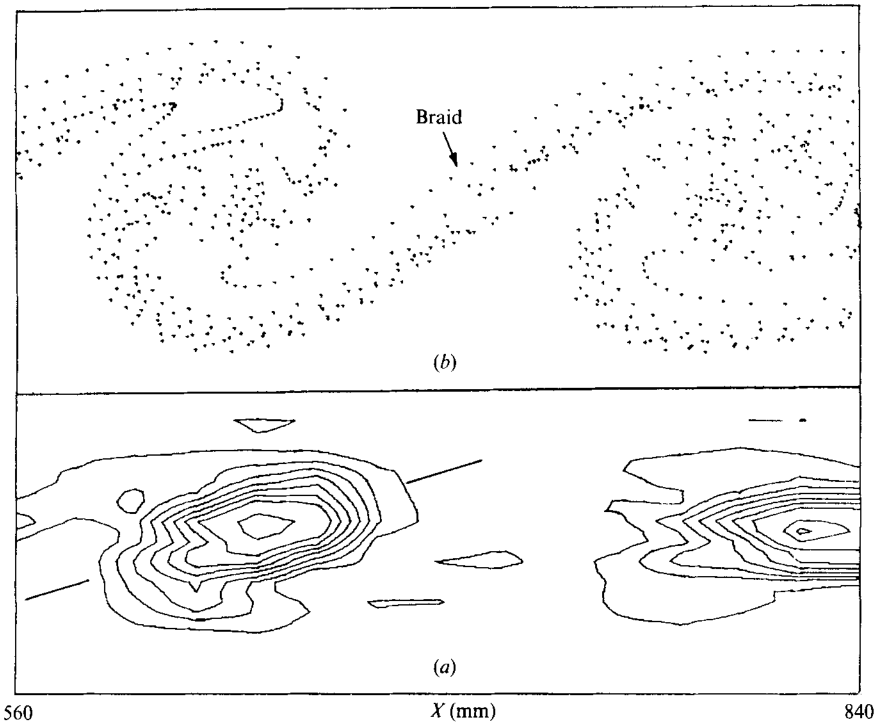

FIGURE 18. The phase-locked structures in region II: (*a*) calculated streaklines; (*b*) calculated isodynes.

motion and the large coherent structures. The corresponding phase-locked vorticity field is also presented in figure 16.

A detailed comparison between the measured vorticity contours and the concomitant streaklines in each of the regions discussed is shown in figures 17–19.

The vorticity in region I is concentrated in two cores, displaced both longitudinally and laterally (figure 17). The longitudinal displacement of these cores diminishes with increasing distance from the flap until it vanishes at the beginning of region II, forming a circular lump. The two cores of vorticity within the circular lump retain their identity for some time ($450 < X < 600$ mm) before merging completely into a single vortex at $X \approx 600$ mm (figures 17 and 18). The isodynes in region II have a single core with a maximum vorticity at its centre. Two cores of the phase-locked vorticity contours reappear in the second transition region ($900 < X < 1100$ mm) and in region III near the end of the test section ($X \approx 1600$ mm). The regeneration of the two cores in the second transition region coincides with a positive contribution to the cross-spectrum of the fluctuations at the fundamental and the harmonic frequency. The vorticity between the cores is stretched by the large vortex lumps and virtually disappears at $X \approx 700$ mm (figures 16 and 18).

The vorticity distribution in regions I and II is consistent with the linear stability theory as discussed in §4 (see also Michalke 1964, 1965). Even the disappearance of the local minimum, while the flow becomes stable to the excitation frequency, corresponds to the lateral location at which $U'' = 0$ and was explained by Michalke (see figures 17 and 18). The concentration of the perturbation vorticity in region III

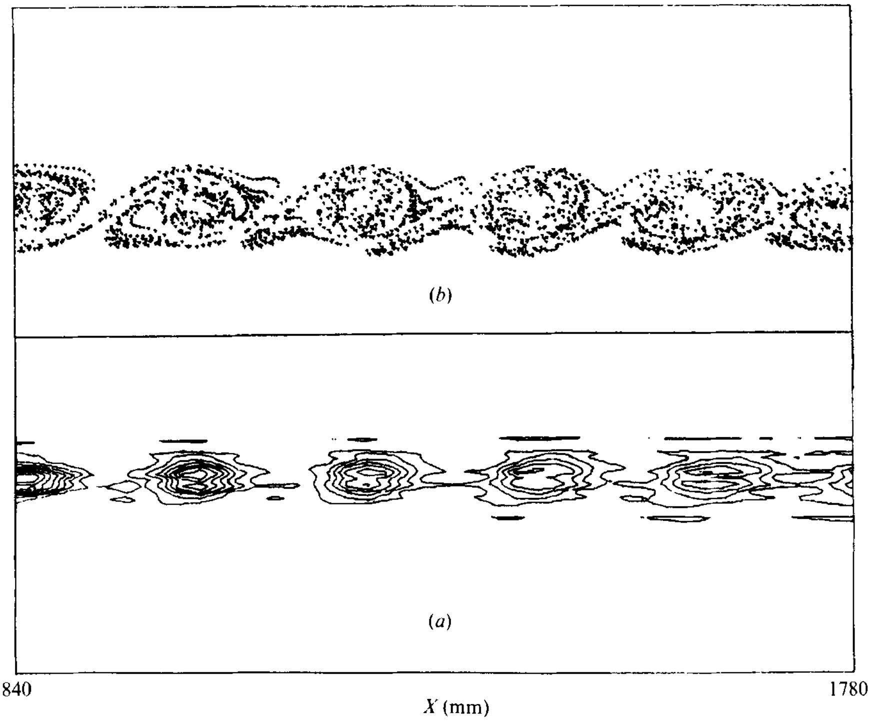

FIGURE 19. The phase-locked structures in region III: (a) calculated streaklines; (b) calculated isodynes.

decreases with increasing X (figure 19), indicating the limitation of the inviscid linear assumption.

The streaklines shown in figure 17 suggest that region I, which is marked by a rapid growth of the shear layer, can be characterized by the amplification of disturbances in the lateral direction. Its length is equal to the distance required for the vortex sheet to roll into a single lumpy structure. A lump (or patch) is formed at the cross-section at which the streakline pattern folds over backward.

The lateral dimension of the vortex lumps in region II remains unchanged (figures 17 and 18), but their inclination to the flow axis is reduced. The inclination of the major axis of the lumps is larger than $\frac{1}{2}\pi$ in region I; it crosses $\frac{1}{2}\pi$ at the beginning of region II and becomes smaller with increasing X. The inclination angle of the large vortices is related to the sign of the Reynolds stress as suggested by Browand & Ho (1983). The thin vortex sheet which separates adjacent lumps, and sometimes is referred to as the 'braid', is stretched in the process, as can be seen from the calculated streaklines.

Neither the phase-locked streaklines, nor the photographs produced by stroboscopic or by single-flash illumination, showed the occurrence of pairing in this experiment. Many single-exposure photographs were taken in order to verify that the stroboscopic illumination used (figure 16) did not suppress the appearance of 'pairing' interactions which might have occurred randomly in time relative to the phase of the flap. These observations spurred an extensive investigation which is discussed separately (Wygnanski & Weisbrot 1988).

7. Conclusions

The transverse distributions of the phase-locked fluctuations are well predicted by the linear stability model in spite of the high amplitudes involved. The model fails to predict accurately the rate of amplification of these disturbances in the direction of streaming and, therefore, a weakly nonlinear perturbation scheme which modifies the rate of amplification with X while retaining the normalized shape of the eigenfunctions may correct these deficiencies (Wygnanski, Marasali & Champagne 1987).

The formation of a significant subharmonic frequency was not observed even in region III, where the width of the shear layer exceeds the wavelength associated with the excitation. On the other hand, the first harmonic frequency was prominent in regions I and II, and there was a continuous exchange of energy between the harmonic and the fundamental throughout these two regions. This process is most clearly observed in the cross-spectra and suggests that a resonance of the Kelly (1967) type may occur between the fundamental frequency and the first harmonic, rather than between the fundamental and its subharmonic.

Conventional techniques of flow visualization did not reveal the existence of 'pairing' or other modes of vortex amalgamation in the present experiment.

The authors wish to express their gratitude to Dr M. Gaster, who introduced them to the linear stability approach in this case, and to Dr E. Kit for his continuous assistance in the experimental work. The work was supported in part by the AFOSR under Grant No. 83-0235.

REFERENCES

ACTON, E. 1976 The modelling of large eddies in a two-dimensional shear layer. *J. Fluid Mech.* **76**, 561.

ASHURST, W. T. 1979 Numerical simulation of turbulent mixing layers via vortex dynamics. In *Turbulent Shear Flows*, vol. 1 (ed. F. Durst, B. E. Launder, F. W. Schmidt & J. H. Whitelaw), p. 402. Springer.

BOUTHIER, M. 1972 Stabilité linéaire des écoulements presque parallèles. *J. Méc.* **11**, 599.

BROWN, G. L. & ROSHKO, A. 1974 On density effects and large structure in turbulent mixing layers. *J. Fluid Mech.* **64**, 775.

BROWAND, F. K. & HO, C. M. 1983 The mixing layer: an example of quasi two-dimensional turbulence. *J. Méc., Numero Special*, p. 99.

BROWAND, F. K. & WEIDMAN, P. D. 1976 Large scales in the developing mixing layer. *J. Fluid Mech.* **76**, 127.

CORCOS, G. M. & SHERMAN, F. S. 1984 The mixing layer: deterministic models of a turbulent flow, part 1. Introduction and the two-dimensional flow. *J. Fluid Mech.* **139**, 29.

CRIGHTON, D. G. & GASTER, M. 1976 Stability of slowly diverging jet flow. *J. Fluid Mech.* **77**, 397.

FIEDLER, H. E. & MENSING, P. 1985 The plane turbulent shear layer with periodic excitation. *J. Fluid Mech.* **150**, 281.

GASTER, M., KIT, E. & WYGNANSKI, I. 1985 Large scale structures in a forced turbulent mixing layer. *J. Fluid Mech.* **150**, 23.

HO, C. M. & HUANG, L. S. 1982 Subharmonics and vortex merging in mixing layers. *J. Fluid Mech.* **119**, 443.

HO, C. M. & HUERRE, P. 1984 Perturbed free shear layers. *Ann. Rev. Fluid Mech.* **16**, 365.

HUSSAIN, A. K. M. F. 1983 Coherent structures – reality and myth. *Phys. Fluids* **26**, 2816.

INOUE, O. & LEONARD, A. 1987 Vortex simulation of forced/unforced mixing layers. *AIAA Paper* 87-0288.

KELLY, R. E. 1967 On the stability of an inviscid shear layer which is periodic in space and time. *J. Fluid Mech.* **27**, 657.

MICHALKE, A. 1964 On the inviscid instability of the hyperbolic tangent velocity profile. *J. Fluid Mech.* **19**, 543.

MICHALKE, A. 1965 Vortex formation in a free boundary layer according to stability theory. *J. Fluid Mech.* **22**, 371.

MONKEWITZ, P. A. & HUERRE, P. 1982 The influence of velocity ratio on the spatial instability of mixing layers. *Phys. Fluids* **25**, 1137.

OSTER, D. & WYGNANSKI, I. 1982 The forced mixing layer between parallel streams. *J. Fluid Mech.* **123**, 91.

OSTER, D., WYGNANSKI, I., DZIOMBA, B. & FIEDLER, H. 1978 The effects of initial conditions on the two-dimensional mixing layer. Lecture Notes in Physics, vol. 75, p. 48.

PATNAIK, P. C., SHERMAN, F. S. & CORCOS, G. M. 1976 A numerical simulation of Kelvin–Helmholtz waves of finite amplitude. *J. Fluid Mech.* **73**, 215.

RILEY, J. J. & METCALFE, R. W. 1980 Direct numerical simulation of a perturbed turbulent mixing layer. *AIAA Paper* 80-0274.

WINANT, C. D. & BROWAND, F. K. 1974 Vortex pairing, the mechanism of turbulent mixing-layer growth at moderate Reynolds number. *J. Fluid Mech.* **63**, 237.

WYGNANSKI, I., FIEDLER, H., OSTER, D. & DZIOMBA, B. 1979 On the perseverance of a quasi two-dimensional eddy structure in a turbulent mixing layer. *J. Fluid Mech.* **93**, 325.

WYGNANSKI, I., MARASALI, B. & CHAMPAGNE, F. 1987 On the weakly nonlinear stability model applied to a diverging small-deficit wake. *AIAA Paper* 87-1465.

WYGNANSKI, I. & WEISBROT, I. 1988 On the pairing process in an excited, plane, turbulent mixing layer. *J. Fluid Mech.* **195**, 161–173.